

1 **The geochemical and geochronological implications of nanoscale trace element clusters**  
2 **in rutile**

3 **R. Verberne<sup>1, 2\*</sup>, S.M. Reddy<sup>1, 2</sup>, D.W. Saxey<sup>2</sup>, D. Fougereuse<sup>1, 2</sup>, W.D.A. Rickard<sup>2</sup>, D.**  
4 **Plavsa<sup>3</sup>, A. Agangi<sup>1, 4</sup>, A.R.C. Kylander-Clark<sup>5</sup>**

5 <sup>1</sup>School of Earth and Planetary Sciences, Curtin University, Perth, WA 6845, Australia

6 <sup>2</sup>Geoscience Atom Probe, Advanced Resource Characterization Facility, John de Laeter  
7 Centre, Curtin University, Perth, WA 6845, Australia

8 <sup>3</sup>Future Industries Institute, University of South Australia, Mawson Lakes, South Australia  
9 5095, Australia

10 <sup>4</sup>Department of Geology, University of Johannesburg, South Africa

11 <sup>5</sup>Department of Earth Science, University of California. Santa Barbara, USA

12 \*e-mail corresponding author: rick.verberne89@gmail.com

13

14 **ABSTRACT**

15 The geochemical analysis of trace elements in rutile (e.g. Pb, U and Zr) is routinely  
16 used to extract information on the nature and timing of geological events. However, the  
17 mobility of trace elements can affect age and temperature determinations with the controlling  
18 mechanisms for mobility still debated. To further this debate, we use laser ablation ICP-MS  
19 and atom probe tomography to characterize the micro- to nanoscale distribution of trace  
20 elements in rutile sourced from the Capricorn Orogen, Western Australia. At the > 20µm  
21 scale, there is no significant trace element variation in single grains and a concordant U-Pb  
22 crystallization age of 1872±6 [36] Ma shows no evidence of isotopic disturbance. At the  
23 nanoscale, clusters up to 20nm in size and enriched in trace elements (Al, Cr, Pb and V) are  
24 observed. The <sup>207</sup>Pb/<sup>206</sup>Pb ratio of 0.176±0.040 (2σ) obtained from clusters indicates that they  
25 formed after crystallization, potentially during regional metamorphism. We interpret the

26 clusters to have formed by the entrapment of mobile trace elements in transient sites of  
27 radiation damage during upper amphibolite-facies metamorphism. The entrapment will affect  
28 the activation energy for volume diffusion of elements present in the cluster. The low number  
29 and density of clusters provides constraints on the time over which clusters formed,  
30 indicating peak metamorphic temperatures are short-lived, <10 Ma, events. Our results  
31 indicate that the use of trace elements to estimate volume diffusion in rutile is more complex  
32 than assuming a homogeneous medium.

33 Keywords: Rutile, Geochronology, Atom Probe Tomography, Nanoscale, Pb clusters

34

## 35 INTRODUCTION

36 Rutile is the stable TiO<sub>2</sub> polymorph at mid- to lower crustal metamorphic conditions  
37 (Dachille et al., 1968) and a common accessory mineral in rocks. The trace element and  
38 isotope composition of rutile provide constraints on mineral provenance (Cr, Nb) (Meinhold,  
39 2010), mineralization (Sn, Sb, V, W) (Agangi et al., 2019; Plavsa et al., 2017), thermal  
40 history (Zr) (Zack et al., 2004) and geochronology (U, Pb) (Mezger et al., 1989).

41 Underpinning the widespread application of rutile geochemistry and geochronology is the  
42 assumption that the mobility of trace elements is well understood. However, studies show  
43 that there are significant gaps in our understanding of trace element systematics.

44 For rutile, a range of values have been proposed for the Pb closure temperature, the minimum  
45 temperature at which Pb is mobile via volume diffusion and can decouple from U, affecting  
46 the geochronometer (Cherniak, 2000; Dohmen et al., 2019). U, Pb and Zr profiles were also  
47 demonstrated to yield different closure temperatures and cooling histories in the same rock  
48 (Kohn et al., 2016; Kooijman et al., 2010; Smye and Stockli, 2014) and the spread of  
49 <sup>206</sup>Pb/<sup>238</sup>U ages (Romer and Rötzler, 2001) resulting from initial isotope heterogeneities.

50 However, the effects of volume diffusion has been questioned during recrystallisation,

51 exsolution or grain-boundary transport (Smye et al., 2018; Zack and Kooijman, 2017).  
52 Nanoscale studies of zircon (Peterman et al., 2016; Reddy et al., 2016; Valley et al., 2014),  
53 pyrite (Fougerouse et al., 2019) and monazite (Fougerouse et al., 2018) illustrate that our  
54 understanding of trace-element distribution is incomplete. The presence of microstructures in  
55 rutile affect diffusion and the trace element composition (Moore et al., 2020) while the effects  
56 of radiation damage in rutile are unknown and likely different from other minerals  
57 (Trachenko et al., 2006).

58 In this paper, we investigate the distribution of Pb and trace elements in rutile by comparing  
59 the composition of metamorphosed U-rich rutile at scales from  $\mu\text{m}$  to nm. The analyses  
60 reveal the presence of Pb clusters and provide constraints on the duration and timing of  
61 cluster formation. The results show a contrast in the distribution of trace elements at varying  
62 length-scales, with potential implications for the way we interpret geochronological and  
63 geochemical data.

64         The study focuses on rutile sourced from quartzite in the Mesoproterozoic Moogie  
65 Metamorphics found in the Mooloo Zone of the Capricorn Orogen of Western Australia (Fig.  
66 1, DR-1). Deposition took place c. 2200 Ma (Cawood and Tyler, 2004) and the area was  
67 affected by multiple metamorphic events including the Capricorn Orogeny (c. 1820 -1770  
68 Ma, 425-500 °C, < 4 kbar), the Mangaroon Orogeny (1680 – 1620 Ma, 600-700 °C, low P),  
69 the Mutherbukin Tectonic Event (c. 1320 – 1170 Ma, >650 °C, 5-6 kbar), the Edmundian  
70 Orogeny (c. 1030 – 955 Ma, 500-550 °C, 3-4 kbar) and the Mulka Tectonic event (c. 570 Ma,  
71 P-T not reported) (Johnson, 2013; Plavsa et al., 2018; Sheppard et al., 2010). However, in  
72 samples sourced from the Mooloo Zone no evidence for events younger than the Capricorn  
73 Orogeny have been reported.

74 The quartzite shows a weak foliation and consists of large, recrystallized quartz grains.

75 Muscovite, rutile, zircon, apatite, sulfides and Fe-oxide occur as accessory minerals. Rutile

76 forms elongated idioblastic to subhedral 200  $\mu\text{m}$  grains, located at quartz grain boundaries.  
77 Small inclusions of zircon are present in a few grains.

78

## 79 RESULTS

80 U-Pb and trace-element compositions were analyzed by Laser-Ablation Split-Stream  
81 Inductively Coupled Plasma Mass Spectrometry (LASS) (Plavsa et al., 2017), DR-2. The  
82 trace-element concentrations vary amongst grains and are reproducible in single grains (DR-  
83 3). Zr-in-rutile thermometry (Watson et al., 2006) yielded temperatures between 637 – 722  
84  $^{\circ}\text{C}$  with an average of 677  $^{\circ}\text{C}$ . The U-Pb isotopic composition yielded a concordant age of  
85  $1872 \pm 6$  [36] Ma ( $2\sigma$ ) ( $N = 32$ , MSWD = 1.12) (Fig. 2). An idioblastic, inclusion-free rutile  
86 (rt9), with a U and Pb composition of 344 and 129 ppm respectively, a concordant age of  
87  $1871 \pm 8$  Ma ( $2\sigma$ ) and T of 719  $^{\circ}\text{C}$  (Watson et al., 2006), was selected for atom probe  
88 tomography (APT) analysis. Four APT specimens were prepared by FIB-SEM using  
89 procedures from (Rickard et al., 2020) and analyzed using a Cameca local electrode atom  
90 probe (LEAP 4000X HR, DR-2, 4). The specimens yielded between 43 - 104 million detected  
91 ions and gave similar mass-to-charge spectra (DR-6) to those from previous APT studies of  
92 rutile (Verberne et al., 2019). The 3D reconstructed data reveal clustering of Pb, Al, Cr and V  
93 within all specimens (Fig 3, DR-7). The clusters have a flattened spheroidal shape, a long  
94 axis of 3-20 nm and a maximum volume of  $770 \text{ nm}^3$ . A total of 46 clusters were identified  
95 and isolated using a 0.05 at.%  $^{206}\text{Pb}^{++}$  isoconcentration surface. Concentration gradients  
96 between the clusters and matrix are shown in a proximity histogram, limited by the short axis  
97 of the smallest cluster (Hellman et al., 2000) (Fig. 3d). Pb reaches concentrations of 1.2 at.%  
98 in the cluster, V goes up to 0.8 at.%, Cr increased from 0.35 to 0.6 at.% and Al increases  
99 from 0.02 to 0.25 at.%. Zr is unaffected and U and Th are not detected within the clusters. No  
100 concentration plateau was reached within the clusters. Increasing trace-element concentration

101 are compensated by a decrease in Ti and O. Approximately 2500  $^{206}\text{Pb}$  atoms and 440  $^{207}\text{Pb}$   
102 atoms were calculated to be present in the clusters for a  $^{207}\text{Pb}/^{206}\text{Pb}$  ratio of  $0.176\pm 0.040$  ( $2\sigma$ )  
103 Fig 3, DR-2,5.

## 104 **DISCUSSION**

### 105 **Nanoscale trace-element clusters**

106 APT analysis of metamorphic rutile reveals heterogeneities in Pb and trace-element  
107 compositions at the nanoscale. Pb, Al, Cr and V are segregated in clusters with no apparent  
108 systematic distribution. The nanoscale clusters have major elemental compositions of  $\text{TiO}_2$   
109 ( $>95$  at.%), with Pb as the dominant trace element component (1.2 at.%). Hence, the clusters  
110 do not represent a mineral inclusion or exsolution (Fougerouse et al., 2018) and are unlikely  
111 to be an inclusion of a precursor phase.

### 112 **Pb isotopic composition**

113 APT allows the Pb isotopic composition of the clusters to be estimated. However,  
114 the precision in this study is compromised by the low Pb counts and an isotopic interference  
115 of the  $^{206}\text{Pb}^{++}$  tail on the  $^{207}\text{Pb}^{++}$  peak, an issue for peaks spaced within  $<1$  Da. Modelling of  
116 the  $^{206}\text{Pb}^{++}$  tail can allow for the estimation of the interfered peak DR-7 (Blum et al., 2018).  
117 This correction increases uncertainty, however, data sets with higher Pb counts and  
118 improvements in detector efficiency will reduce this effect significantly. Assuming the Pb  
119 isotope measurements are concordant, the  $^{207}\text{Pb}/^{206}\text{Pb}$  ratio of  $0.176\pm 0.040$  ( $2\sigma$ ) corresponds  
120 to an age between 2180-2950 Ma, older than the crystallization age of  $1871\pm 8$  Ma ( $2\sigma$ ) Ma.  
121 U is not detected in the clusters and so the  $^{207}\text{Pb}/^{206}\text{Pb}$  ratio has not evolved by radiogenic  
122 decay. This implies that the clusters record the  $^{207}\text{Pb}/^{206}\text{Pb}$  ratio at the time of cluster  
123 formation. The timing of segregation can be calculated using the crystallization age and the  
124  $^{207}\text{Pb}/^{206}\text{Pb}$  ratio of the clusters (Peterman et al., 2016; Valley et al., 2014). Here, we a single  
125 age or event cannot be pinpointed due to the low Pb counts resulting in large uncertainties

126 (0.176±0.040) (2σ). However, the Pb isotopic composition of the clusters indicate that cluster  
127 formation and trace element mobility is a secondary process. This process modified trace  
128 element distributions resulting in heterogeneities not observable at the micron scale. The  
129 LASS data therefore represents a mix of multiple discrete reservoirs and can potentially  
130 affect the application of rutile geochemistry and geochronology.

### 131 **Mechanism for nanocluster formation**

132 The clusters have a spheroidal shape with no obvious systematic spatial distribution Fig 3b.  
133 Previous studies have associated the presence of a radiogenic Pb-component in clusters with  
134 the damage caused during radioactive decay, providing sites for cluster formation (Valley et  
135 al., 2014) and enhanced diffusion pathways (Peterman et al., 2016; Valley et al., 2014). In  
136 rutile, the formation and recovery of radiation damage is two-fold. A decay event results in a  
137 small core of highly disordered lattice that slowly recovers and a region with less distortion  
138 that instantly recovers by  $\alpha$ -healing due to the low, critical amorphization temperature of  
139 rutile (Trachenko et al., 2006). Unlike in zircon, this inhibits the build-up of radiation  
140 damage, preventing long-range connectivity, limiting Pb migration at low temperatures  
141 (Cherniak). However, metamorphic temperatures measured in the Capricorn region are near  
142 the closure temperature for Pb diffusion in rutile (480-630 °C, (Cherniak, 2000; Plavsa et al.,  
143 2018)) these temperatures allow for ample, short-distance, Pb migration.

144         The formation of Pb clusters in zircon and pyrite has led to the recognition of three  
145 models that describe the mechanism of cluster formation under different conditions. Pb  
146 clusters in pyrite were explained via the entanglement of dislocations (Fougerouse et al.,  
147 2019), with Pb migration along the dislocation. The formation of toroidal-shaped Pb clusters  
148 in zircon was explained via the entrapment of Pb in dislocation-loops, following the build-up  
149 of radiation damage due to U-decay past the first percolation point and subsequent  
150 recrystallisation (Peterman et al., 2016). The third model is related to  $\alpha$ -recoil, involving

151 short-distance (nm's) volume diffusion at high temperatures into regular spaced radiation-  
152 damaged sites. The observations in this study do not fit with these models as there is no  
153 apparent systematic distribution of cluster as observed in (Valley et al., 2014).

154 Using the number of clusters, LASS U-Pb data and assuming each U decay chain  
155 results in the formation of one cluster, we calculate that 46 clusters can form in 3-4 million  
156 years. This process would be faster if each of the 7 or 8  $\alpha$ -emissions of the U decay chain  
157 results in a cluster. Assuming similar daughter recoil distances as in zircon, 20-40 nm spaced  
158 clusters would be expected (Valley et al., 2015). In our data, > 75% of the clusters are  $\geq 40$   
159 nm apart with a median of c. 50nm (Fig 3c).

160 Considering the rutile yields concordant ages and is homogeneous at the micro-  
161 scale, the theoretical amount of Pb, based on LASS, present within all APT specimens at the  
162 onset of the latest high-grade metamorphic event, the Mutherbukin Tectonic Event, was  
163 estimated to c. 3050 Pb atoms (DR-5). This estimated figure is similar to the c. 2940 Pb  
164 atoms measured in the clusters suggesting that all Pb moved into discrete domains at that  
165 time.

166 For the formation of clusters in rutile, we therefore propose that Pb, Al, Cr and V  
167 were trapped in transient radiation damage cores shortly after a decay event (Fig 4). The  
168 small number of clusters requires the cluster-formation event to be limited to a narrow  
169 temperature/time window. When decay occurs at temperatures sufficiently high to enable  
170 trace element diffusion, the final Pb forming event can result in a single cluster without being  
171 obliterated by a next event in the chain.

## 172 **Implications for trace element analysis and geochronology of rutile**

173 The results show a discrepancy in our ability to detect element mobility at different length  
174 scales. The LASS data yields concordant ages and consistent concentrations at the grain scale  
175 indicating no evidence for heterogeneous Pb distribution and therefore assumed to be

176 immobile at the  $> 10 \mu\text{m}$  scale. In contrast, the APT data shows heterogeneous trace-element  
177 and Pb compositions at the nanoscale. This may limit the application of techniques to  
178 precisely measure U-Pb ages in rutile, a point recently illustrated for zircon via scanning ion-  
179 imaging (Ge et al., 2018).

180 The agreement between the empirical and measured Pb atom count in the clusters suggest it  
181 is likely that the formation of clusters was linked to the latest tectonothermal event known to  
182 have affected the wider region, despite large uncertainties associated with the APT data. As  
183 shown for zircon (Peterman et al., 2016; Valley et al., 2014), the formation of clusters with  
184 discrete isotopic compositions provides additional information on the timing of geological  
185 events that cannot be measured by larger volume analytical techniques. The results indicate  
186 that rutile may also record evidence for geological events that only manifest at the nanoscale.  
187 The segregation of trace elements into clusters will have two important effects on the  
188 diffusion characteristics of those elements within rutile. Firstly, segregation represents a  
189 minimization of free energy. For a cluster to be stable clustered elements must be in a lower  
190 energy configuration. The activation energy for volume diffusion from the clusters is  
191 theoretically higher than the activation energy for diffusion through the lattice. Furthermore,  
192 at temperature conditions sufficient for diffusion, the clusters represent low energy sites that  
193 may trap diffusing trace elements. The tendency of a system to be in a low energy  
194 configuration also explains the differences observed between the trace elements. Low energy  
195 configurations are based on composition and the site trace elements occupy (Sayle et al.,  
196 1995). For example, Sayle et al. (1994) demonstrated  $\text{Al}^{3+}$  will affect the  $\text{Nb}^{5+}$  distribution in  
197 Nb-doped  $\text{TiO}_2$  concluding it may affect diffusion characteristics due to occupying an  
198 interstitial site instead of the more reactive  $\text{Ti}^{3+}$ .

199 Geological scenarios where a second thermal event occurs after cluster formation  
200 can be envisaged. The subsequent entrapment of Pb in earlier formed clusters would result in

201 mixed isotopic compositions. Data collected from conventional analytical techniques (5-  
202 100µm spatial resolution) may incur erroneous geological interpretations if solely based on  
203 volume diffusion-controlled concentrations of trace elements as these will be affected by the  
204 presence of clusters.

## 205 **ACKNOWLEDGEMENTS**

206 The work was conducted within the Geoscience Atom Probe Facility, Curtin University, part  
207 of the Advanced Resource Characterization Facility (ARCF). The ARCF, under the auspices  
208 of the National Resource Sciences Precinct (NRSP). A collaboration between CSIRO, Curtin  
209 University, and The University of Western Australia supported by the Science and Industry  
210 Endowment Fund (SIEF). The authors gratefully acknowledge support of Curtin University's  
211 Microscopy & Microanalysis Facility and the John de Laeter Centre, whose instrumentation  
212 has been supported by University, State and Commonwealth Government funding. We would  
213 also like to thank J. Valley, R. Holder, T. Zack and the anonymous reviewers for their  
214 feedback.

215

216 Fig.1: a) Simplified geological map after (Plavsa et al., 2018), (DR-1). Red star indicates  
217 sample location. b) SE image of the rutile grain analyzed by LASS-ICP-MS and APT  
218 showing the laser spots and the APT lift out sections. The LASS spot size is 30µm

219

220 Fig.2: Tera-Wasserburg plot showing the rutile ages for thin section 216806, with the data of  
221 the grain analyzed by APT in red.

222

223 Fig.3: a: Images of the 4 APT reconstructions showing the Pb clusters (DR-7). b) Image of  
224 one of the Pb clusters showing the distribution of  $^{206}\text{Pb}$  and  $^{207}\text{Pb}$ . c: Box plots showing the  
225 nearest-neighbor distribution of the individual specimens and combined values (red), number

226 of clusters is given in brackets. d: Proximity histogram based upon all 46 Pb-clusters showing  
227 the profile of Pb, Al, Cr, Nb, V, W and Zr, error bars are  $1\sigma$ .

228

229 Fig.4: Schematic model for the formation of Pb clusters in rutile based on radiation damage  
230 experiments (Trachenko et al., 2006). a:  $\alpha$ -Decay creates two radiation damage zones. b:

231 Dilute damage recovers instantly due to  $\alpha$ -healing. c: Within a limited temperature window

232 Pb can migrate over short distances in the severely damaged zone. If temperatures are too

233 low, there will be no migration and the damage will recover over time. If temperatures are

234 higher Pb loss might occur and the damage recovery would be faster.

235

236

237

238 Agangi, A., Reddy, S. M., Plavsa, D., Fougereuse, D., Clark, C., Roberts, M., and Johnson, T. E., 2019,  
239 Antimony in rutile as a pathfinder for orogenic gold deposits: *Ore Geology Reviews*, v. 106,  
240 p. 1-11.

241 Blum, T. B., Reinhard, D. A., Chen, Y., Prosa, T. J., Larson, D. J., and Valley, J. W., 2018, Uncertainty  
242 and Sensitivity Analysis for Spatial and Spectral Processing of Pb Isotopes in Zircon by Atom  
243 Probe Tomography: *Microstructural Geochronology: Planetary Records Down to Atom Scale*,  
244 p. 327-350.

245 Cawood, P. A., and Tyler, I. M., 2004, Assembling and reactivating the Proterozoic Capricorn Orogen:  
246 lithotectonic elements, orogenies, and significance: *Precambrian Research*, v. 128, no. 3-4, p.  
247 201-218.

248 Cherniak, D., 2000, Pb diffusion in rutile: *Contributions to Mineralogy and Petrology*, v. 139, no. 2, p.  
249 198-207.

250 Dacheville, F., Simons, P., and Roy, R., 1968, Pressure-temperature studies of anatase, brookite, rutile  
251 and TiO<sub>2</sub>-II: *Am Mineral*, v. 53, p. 1929-1939.

252 Dohmen, R., Marschall, H. R., Ludwig, T., and Polednia, J., 2019, Diffusion of Zr, Hf, Nb and Ta in  
253 rutile: effects of temperature, oxygen fugacity, and doping level, and relation to rutile point  
254 defect chemistry: *Physics and Chemistry of Minerals*, v. 46, no. 3, p. 311-332.

255 Fougereuse, D., Reddy, S. M., Kirkland, C. L., Saxey, D. W., Rickard, W. D., and Hough, R. M., 2019,  
256 Time-resolved, defect-hosted, trace element mobility in deformed Witwatersrand pyrite:  
257 *Geoscience Frontiers*, v. 10(1), p. 55-63.

258 Fougereuse, D., Reddy, S. M., Saxey, D. W., Erickson, T. M., Kirkland, C. L., Rickard, W. D. A., Seydoux-  
259 Guillaume, A. M., Clark, C., and Buick, I. S., 2018, Nanoscale distribution of Pb in monazite  
260 revealed by atom probe microscopy: *Chemical Geology*, v. 479, p. 251-258.

261 Ge, R., Wilde, S. A., Nemchin, A. A., Whitehouse, M. J., Bellucci, J. J., Erickson, T. M., Frew, A., and  
262 Thern, E. R., 2018, A 4463 Ma apparent zircon age from the Jack Hills (Western Australia)  
263 resulting from ancient Pb mobilization: *Geology*, v. 46, no. 4, p. 303-306.

264 Hellman, O. C., Vandenbroucke, J. A., Rusing, J., Isheim, D., and Seidman, D. N., 2000, Analysis of  
265 Three-dimensional Atom probe Data by the Proximity Histogram: *Microsc Microanal*, v. 6,  
266 no. 5, p. 437-444.

267 Johnson, S. P., 2013, The birth of supercontinents and the Proterozoic assembly of Western  
268 Australia, *AusIMM Bulletin*, Geological Survey of Western Australia.

269 Kohn, M. J., Penniston-Dorland, S. C., and Ferreira, J. C., 2016, Implications of near-rim compositional  
270 zoning in rutile for geothermometry, geospeedometry, and trace element equilibration:  
271 *Contributions to Mineralogy and Petrology*, v. 171, no. 10, p. 78.

272 Kooijman, E., Mezger, K., and Berndt, J., 2010, Constraints on the U-Pb systematics of metamorphic  
273 rutile from in situ LA-ICP-MS analysis: *Earth and Planetary Science Letters*, v. 293, no. 3-4, p.  
274 321-330.

275 Meinhold, G., 2010, Rutile and its applications in earth sciences: *Earth-Science Reviews*, v. 102, no. 1-  
276 2, p. 1-28.

277 Mezger, K., Hanson, G., and Bohlen, S., 1989, High-precision UPb ages of metamorphic rutile:  
278 application to the cooling history of high-grade terranes: *Earth and Planetary Science*  
279 *Letters*, v. 96, no. 1-2, p. 106-118.

280 Moore, J., Beinlich, A., Porter, J. K., Talavera, C., Berndt, J., Piazzolo, S., Austrheim, H., and Putnis, A.,  
281 2020, Microstructurally controlled trace element (Zr, U–Pb) concentrations in metamorphic  
282 rutile: An example from the amphibolites of the Bergen Arcs: *Journal of Metamorphic*  
283 *Geology*, v. 38, no. 1, p. 103-127.

284 Peterman, E. M., Reddy, S. M., Saxey, D. W., Snoeyenbos, D. R., Rickard, W. D., Fougereuse, D., and  
285 Kylander-Clark, A. R., 2016, Nanogeochronology of discordant zircon measured by atom  
286 probe microscopy of Pb-enriched dislocation loops: *Sci Adv*, v. 2, no. 9, p. e1601318.

287 Plavsa, D., Reddy, S. M., Agangi, A., Clark, C., Kylander-Clark, A., and Tiddy, C. J., 2017,  
288 Microstructural, trace element and geochronological characterization of TiO<sub>2</sub> polymorphs  
289 and implications for mineral exploration: *Chemical Geology*, no. 476, p. 130-149.

290 Plavsa, D., Reddy, S. M., Clark, C., and Agangi, A., 2018, Capricorn Orogen rutile study, a combined  
291 electron backscatter diffraction (EBSD) and laser ablation split stream (LASS) analytical  
292 approach, *Record* 2018/12, 54p.

293 Reddy, S. M., van Riessen, A., Saxey, D. W., Johnson, T. E., Rickard, W. D. A., Fougereuse, D., Fischer,  
294 S., Prosa, T. J., Katherine, P. R. E., Reinhard, D. A., Chen, Y. M., and Olson, D., 2016,  
295 Mechanisms of deformation-induced trace element migration in zircon resolved by atom  
296 probe and correlative microscopy: *Geochimica Et Cosmochimica Acta*, v. 195, p. 158-170.

297 Rickard, W. D., Reddy, S. M., Saxey, D. W., Fougereuse, D., Daly, L., Peterman, E. M., Timms, N.,  
298 Cavosie, A. J., and Jourdan, F., 2020, Novel Applications of FIB-based ToF-SIMS in Atom  
299 Probe Tomography Workflows: *Microscopy and Microanalysis*.

300 Romer, R. L., and Rötzler, J., 2001, P–T–t evolution of ultrahigh-temperature granulites from the  
301 Saxon Granulite Massif, Germany. Part II: geochronology: *Journal of Petrology*, v. 42, no. 11,  
302 p. 2015-2032.

303 Sayle, D., Catlow, C., Perrin, M., and Nortier, P., 1995, Computer simulation study of the defect  
304 chemistry of rutile TiO<sub>2</sub>: *Journal of Physics and Chemistry of Solids*, v. 56, no. 6, p. 799-805.

305 Sheppard, S., Johnson, S., Wingate, M., Kirkland, C., and Pirajno, F., 2010, Explanatory notes for the  
306 Gascoyne Province: Geological Survey of Western Australia, p. 1-336.

307 Smye, A. J., Marsh, J., Vermeesch, P., Garber, J., and Stockli, D., 2018, Applications and limitations of  
308 U-Pb thermochronology to middle and lower crustal thermal histories: *Chemical Geology*, v.  
309 494, p. 1-18.

310 Smye, A. J., and Stockli, D. F., 2014, Rutile U-Pb age depth profiling: A continuous record of  
311 lithospheric thermal evolution: *Earth and Planetary Science Letters*, v. 408, p. 171-182.

312 Trachenko, K., Dove, M. T., Artacho, E., Todorov, I. T., and Smith, W., 2006, Atomistic simulations of  
313 resistance to amorphization by radiation damage: *Physical Review B*, v. 73, no. 17, p. 15.

- 314 Valley, J. W., Cavosie, A. J., Ushikubo, T., Reinhard, D. A., Lawrence, D. F., Larson, D. J., Clifton, P. H.,  
315 Kelly, T. F., Wilde, S. A., and Moser, D. E., 2014, Hadean age for a post-magma-ocean zircon  
316 confirmed by atom-probe tomography: *Nature Geoscience*, v. 7, no. 3, p. 219-223.
- 317 Valley, J. W., Reinhard, D. A., Cavosie, A. J., Ushikubo, T., Lawrence, D. F., Larson, D. J., Kelly, T. F.,  
318 Snoeyenbos, D. R., and Strickland, A., 2015, Nano- and micro-geochronology in Hadean and  
319 Archean zircons by atom-probe tomography and SIMS: New tools for old minerals: *American*  
320 *Mineralogist*, v. 100, no. 7, p. 1355-1377.
- 321 Verberne, R., Saxey, D. W., Reddy, S. M., Rickard, W. D., Fougereuse, D., and Clark, C., 2019, Analysis  
322 of Natural Rutile (TiO<sub>2</sub>) by Laser-assisted Atom Probe Tomography: *Microscopy and*  
323 *Microanalysis*, p. 1-8.
- 324 Watson, E. B., Wark, D. A., and Thomas, J. B., 2006, Crystallization thermometers for zircon and  
325 rutile: *Contributions to Mineralogy and Petrology*, v. 151, no. 4, p. 413-433.
- 326 Zack, T., and Kooijman, E., 2017, Petrology and geochronology of rutile: *Reviews in Mineralogy and*  
327 *Geochemistry*, v. 83, no. 1, p. 443-467.
- 328 Zack, T., Moraes, R., and Kronz, A., 2004, Temperature dependence of Zr in rutile: empirical  
329 calibration of a rutile thermometer: *Contributions to Mineralogy and Petrology*, v. 148, no.  
330 4, p. 471-488.

331

332

333

334

335

Figure 1 - Geological Map

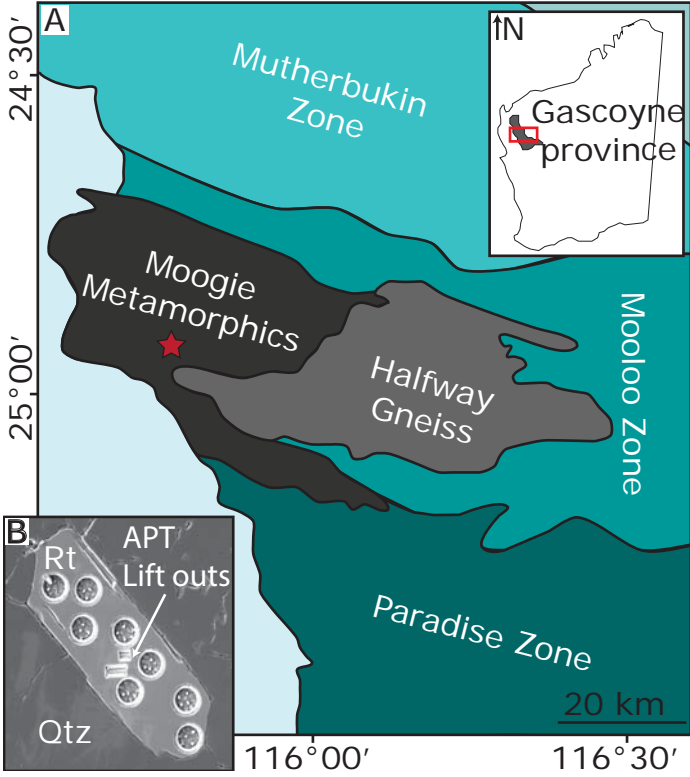
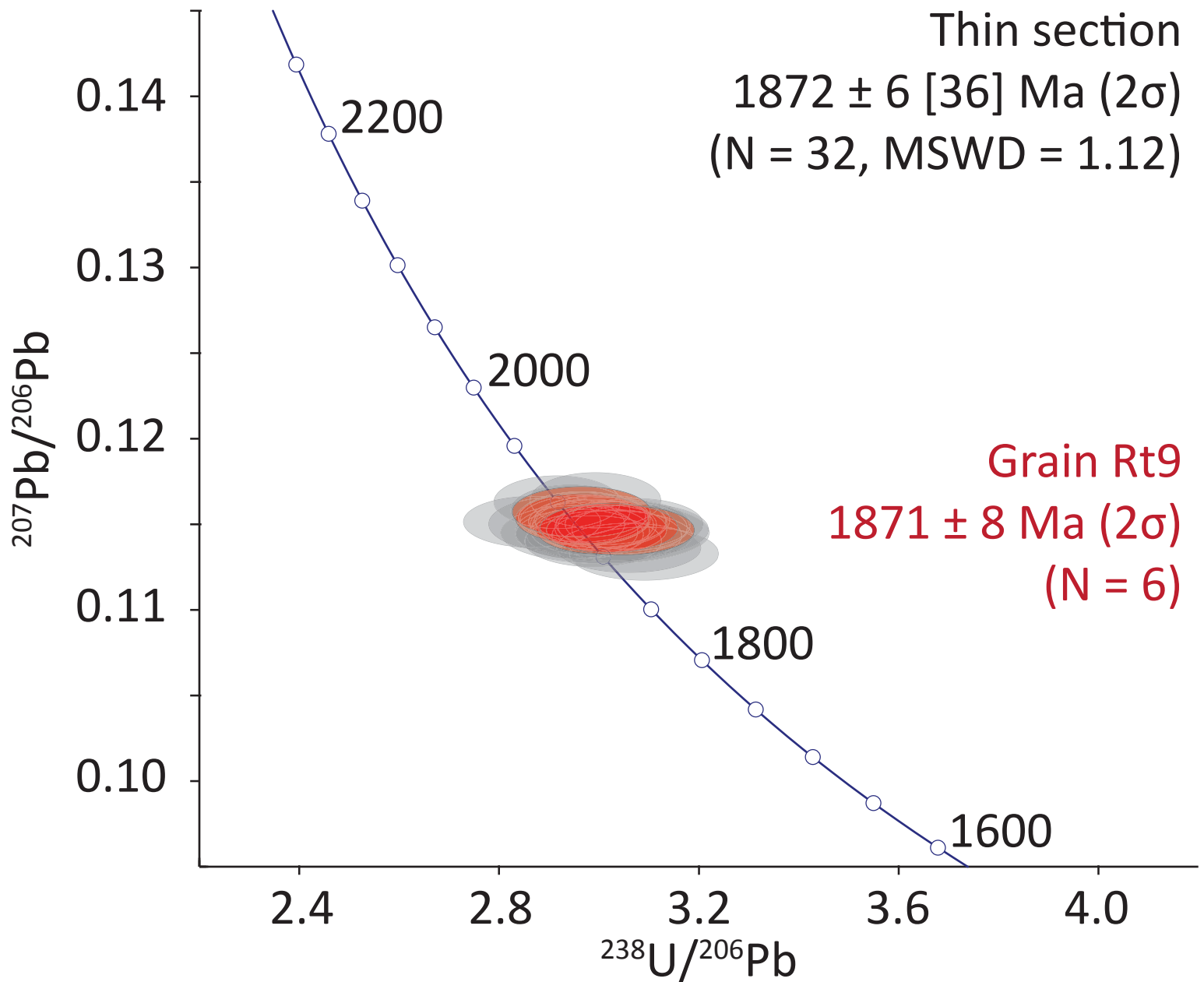
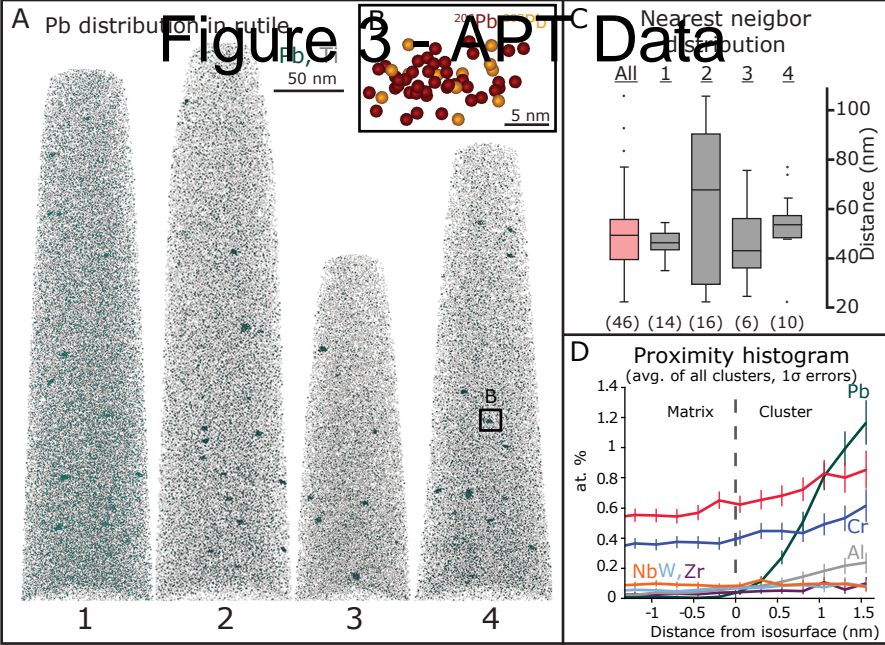


Figure 2 - Tera-Wasserburg diagram





# Figure 4 - Cluster formation model

